

Article

Fine-Grained Tb₃Al₅O₁₂ Transparent Ceramics Prepared by Co-Precipitation Synthesis and Two-Step Sintering

Lixuan Zhang^{1,2}, Xiaoying Li^{1,2}, Dianjun Hu^{1,2}, Mariya Dobrotvorska³, Roman Yavetskiy³, Zhengfa Dai¹, Tengfei Xie¹, Qiang Yuan¹, Haohong Chen¹, Qiang Liu⁴ and Jiang Li^{1,2,*} 

¹ Transparent Ceramics Research Center, Shanghai Institute of Ceramics, Chinese Academy of Sciences, Shanghai 201899, China

² Center of Materials Science and Optoelectronics Engineering, University of Chinese Academy of Sciences, Beijing 100049, China

³ Institute for Single Crystals of NAS of Ukraine, 60 Nauky Ave., 61072 Kharkiv, Ukraine

⁴ School of Material Science and Engineering, Jiangsu University, Zhenjiang 212013, China

* Correspondence: lijiaing@mail.sic.ac.cn; Tel.: +86-21-6916-3689; Fax: +86-21-6990-6700

Abstract: In recent years, transparent terbium aluminum garnet (TAG) ceramics have attracted much attention for use in high-power Faraday isolators. Fine-grained ceramics usually possess better mechanical properties and accordingly better service performance. In this work, transparent TAG ceramics with fine grains were prepared using a two-step sintering procedure based on the low-temperature sintering process to suppress grain growth. The composition of TAG precursor and powders calcined at different temperatures was studied in detail. The microstructure and relative density of air pre-sintered TAG ceramics were studied to meet the requirements of hot isostatic pressing (HIP) post-treatment. Driven by the low pre-sintering temperature in air, the average grain sizes of the obtained TAG ceramics after HIP treatment are about 2.9–5.3 μm. The TAG ceramics (1.2 mm thick) pre-sintered at 1450 °C with HIP post-treatment at 1550 °C for 3 h under a 176 MPa Ar atmosphere possess the highest in-line transmittance of 80.3% at 1064 nm. The Verdet constant of the TAG ceramics at 632.8 nm is $-180.5 \text{ rad} \cdot \text{T}^{-1} \cdot \text{m}^{-1}$ at room temperature, which is about 1.3 times larger than that of the commercial Tb₃Ga₅O₁₂ single crystals.

Keywords: magneto-optical ceramics; TAG ceramics; fine grain; co-precipitation method; hot isostatic pressing



Citation: Zhang, L.; Li, X.; Hu, D.; Dobrotvorska, M.; Yavetskiy, R.; Dai, Z.; Xie, T.; Yuan, Q.; Chen, H.; Liu, Q.; et al. Fine-Grained Tb₃Al₅O₁₂ Transparent Ceramics Prepared by Co-Precipitation Synthesis and Two-Step Sintering. *Magnetochemistry* **2023**, *9*, 47. <https://doi.org/10.3390/magnetochemistry9020047>

Academic Editor: Dmitry Alexandrovich Filippov

Received: 30 December 2022

Revised: 26 January 2023

Accepted: 30 January 2023

Published: 1 February 2023



Copyright: © 2023 by the authors. Licensee MDPI, Basel, Switzerland. This article is an open access article distributed under the terms and conditions of the Creative Commons Attribution (CC BY) license (<https://creativecommons.org/licenses/by/4.0/>).

1. Introduction

Faraday isolators based on the non-reciprocal effect have been widely used in laser systems. The main applications include back-reflections isolation, multi-path scheme organization of laser amplifiers, and thermal birefringence compensation in active laser elements [1–6]. In pace with the development of magneto-optical devices towards high power, miniaturization, and low cost, more stringent requirements are being placed on the properties of magneto-optical materials, such as high Verdet constant, large size, prominent optical quality, high thermal conductivity, superior laser damage threshold, and so on [7–14]. Terbium aluminum garnet (TAG) material has nearly the same transmittance windows and crystal structure as Terbium Gallium Garnet (TGG) single crystal, and has a Verdet constant of about 30% higher than TGG single crystals, so TAG is considered to be a more suitable magneto-optic medium for high power optical isolators [15–18]. However, due to the incongruent melting nature of TAG, it is difficult to grow TAG single crystals with large size and high optical quality, though, in recent years, many researchers have made various attempts to grow TAG single crystals from the aspects of growth method and lattice stability [19–21]. TAG transparent ceramics not only possess excellent performance, similar to single crystals, but also have the advantages of ceramics such as superior size

scalability, excellent thermal properties, and moderate preparation cost [10,17,18,22–26]. Therefore, TAG transparent ceramics provide a perfect choice for magneto-optical isolators.

Because of the continuous improvement in laser power and laser energy, the mechanical properties of magneto-optical ceramics have become a concern. Superior mechanical properties are favorable for ceramics to withstand the energy and heat shock of high-power lasers. In addition, good mechanical properties and damage tolerance are of great significance to the reliability and machinability of ceramics [27]. Many reports have shown that the mechanical properties of transparent ceramics are closely related to their grain size and reducing grain size can improve mechanical properties [28,29]. Therefore, it is worth studying refining the grain size of TAG ceramics on the premise of ensuring the good optical quality of TAG ceramics.

At present, TAG transparent ceramics can be fabricated by two main methods. One is the solid-state reactive sintering from commercial oxide powders [30–32]. Generally, commercial powders have large particle sizes (or serious aggregation), wide particle size distribution, and poor sinterability. Hence, a high sintering temperature and long holding time are needed to obtain transparent TAG ceramics, resulting in an average grain size of more than 10 μm . The second method is vacuum sintering combined with hot isostatic pressing (HIP) post-treatment from co-precipitated TAG powders [10,33–36]. The powders prepared by the co-precipitation method have nanoscale or submicronic size and excellent element uniformity, hence the co-precipitated TAG powders have high sinterability. However, the average grain size of the obtained TAG ceramics can reach up to about 20 μm under the action of high sintering temperature. Coarse grains will seriously reduce the mechanical strength of TAG ceramics, and thus deteriorate the thermal shock fracture resistance of TAG ceramics when applied in high-power laser systems [7,37]. Various new production methods for garnet ceramics have emerged, such as electron-beam-assisted synthesis [38], vacuum sintering combined with HIP post-treatment of powders synthesized by flame spray pyrolysis [39], self-propagating high-temperature synthesis of powders followed by sintering method [40], and so on. However, these production methods are rarely conducted for TAG ceramics. The grain size of transparent ceramics is most sensitive to the sintering temperature and dwelling time, so reducing the sintering temperature and shortening the dwelling time as much as possible are the keys to preparing transparent TAG ceramics with fine grains.

Hot isostatic pressing is widely used for the post-treatment of ceramics to eliminate the residual pores and further realize fully dense transparent ceramics. To eliminate pores as much as possible during HIP post-treatment, it is vital that there are no open pores in the pre-sintered ceramics. This usually means that the relative density of the pre-sintered ceramics must be over 92%. During the stage of solid-state densification for HIP post-treatment, the densification rate is determined by either Nabarro–Herring or Coble creep, according to the following equation [41]:

$$\frac{d(\Delta\rho/\rho)}{dt} = 31.5 \frac{\Omega}{kTG^2} (1 - \rho) \left[D_v + \frac{\pi\delta D_b}{G} \right] \sigma_a \quad (1)$$

where Ω is the molar volume, k is the Boltzmann constant, T is the absolute temperature, G is the mean grain size, ρ is the relative density, D_v is the volume diffusion coefficient, D_b is the boundary diffusion coefficient, δ is the boundary thickness, and σ_a is the applied isostatic stress. From Equation (1), we can find that the densification rate is inversely proportional to the average grain size. By using pre-sintered ceramics with fine grains, the HIP post-treatment can provide a high driving force for densification, allowing the transparency of TAG ceramics at relatively low temperatures and in short time scales.

As vacuum sintering is a common process in TAG productions, oxygen vacancies are an unavoidable point defect in TAG ceramics. Oxygen vacancies usually produce an absorption band in the visible or ultraviolet region [42], so they worsen the optical quality and are unfavorable for the Faraday isolator application. During vacuum sintering, the oxygen in the crystal lattice evaporates as molecular species O_2 , thus creating oxygen vacancies [43].

As a result, air annealing at high temperatures and for long time scales is necessary to eliminate oxygen vacancies [25]. However, for ceramics after HIP post-treatment, the compressed pores produced during HIP treatment may expand after annealing and reduce the optical transparency at shortwave [28]. Sintering in an oxygen-rich atmosphere such as air may be a good choice to reduce the concentration of oxygen vacancies in TAG ceramics.

In this work, a TAG precursor is synthesized by the co-precipitation method. The decomposition process of the precursor is analyzed, and the appropriate calcination temperature of TAG powders is determined. The evolution process of microstructure and relative density of TAG ceramics pre-sintered in air at different temperatures are concerned, and the influences of pre-sintering temperature on the optical quality and microstructure of TAG ceramics are systematically studied.

2. Materials and Methods

2.1. Materials

Tb₄O₇ (99.995%, Golden Dragon Rare-earth Co., Ltd., Longyan, China, the average particle size is about 3 μm), Al(NO₃)₃·9H₂O (99.995%, Aladdin Industrial Corporation, Shanghai, China), NH₄HCO₃ (99.995%, Aladdin Industrial Corporation, Shanghai, China), (NH₄)₂SO₄ (Analytical grade, Sinopharm Chemical Reagent Co., Ltd., Shanghai, China), high-purity concentrated nitric acid (G3, Shanghai Aoban Technology Co., Ltd., Shanghai, China), and tetraethyl orthosilicate (TEOS, 99.999%, Alfa Aesar, Shanghai, China) were used as raw materials.

2.2. Methods

TAG powders were synthesized via a co-precipitation method. Tb(NO₃)₃ solution was prepared by dissolving Tb₄O₇ powder in high-purity hot nitric acid. Al(NO₃)₃ solution was obtained by dissolving Al(NO₃)₃·9H₂O in deionized water. The respective nitrate solutions were mixed in accordance with the chemical formula of Tb₃Al₅O₁₂. NH₄HCO₃ solution with a concentration of 1.5 mol/L was used as the precipitant and (NH₄)₂SO₄ solution as the dispersant was added to the precipitant. The precipitation reaction was conducted by the reverse-strike technique with a dripping speed of 20 mL/min at room temperature. After aging, the precipitate was washed with deionized water and ethanol, and then oven-dried at 70 °C to obtain the precursor, which was subsequently calcined at 1100 °C for 4 h in a muffle furnace. The calcined powders were ball-milled (ND7-2L planetary ball mill, NDTZ, Nanjing, China) for 12 h with ethanol in a zirconia jar containing 10 mm diameter zirconia balls using 0.5 wt% TEOS as a sintering aid. Then, the powders were uniaxially dry-pressed into pellets at 40 MPa followed by cold isostatic pressing at 250 MPa. The relative density of obtained green bodies was about 50%. After that, the green bodies were densified using a two-step sintering procedure: air pre-sintered at 1400–1475 °C for 3 h and then HIP post-treated at 1550 °C for 3 h under 176 MPa (AIP10-30H HIP furnace, AIP, New York, NY, USA). Finally, the TAG ceramics were annealed at 1000 °C for 10 h in air and polished to 1.2 mm on both surfaces for subsequent testing.

2.3. Characterization

X-ray photoelectron spectra of the samples were measured by the high vacuum double-chamber system (XPS, Omicron, Germany) with a hemispherical electrostatic analyzer. The vacuum degree in camera was 10⁻⁷ Pa. The radiation energy was 1253.6 eV (Mg Kα), and the accuracy of the binding energy determination is 0.2 eV. Electron binding energy calibration (E_b) was performed based on the intrinsic standard method with the C 1s level from adsorbed hydrocarbon contamination (E_b = 285 eV) as a reference. The thickness of the analyzed layer was about 5 nm. The sample surface composition was determined using the photoelectron lines area ratio taking into account their sensitivity factors. The errors of absolute values of element atomic concentration, calculated without using etalons, may be up to 30%. Thermogravimetry and differential thermal analysis (TG-DTA) of the precursor were conducted in a TG-DTA analyzer (STA 449 F3, NETZSCH,

Waldkraiburg, German) in air with a heating rate of 10 °C/min. The crystalline phases of the precursor and synthesized powders were identified by X-ray diffraction (XRD, D8 Advance, Bruker AXS GMBH, German). The XRD patterns were recorded with Cu ($K\alpha_1$, $\lambda = 1.542 \text{ \AA}$) radiation in the angular range of $2\theta = 10\text{--}80^\circ$. The morphology of the precursor, powder, and microstructure of the thermally etched surfaces of the TAG ceramics were observed by field emission scanning electron microscopy (FESEM, S-U8220, Hitachi, Japan). In-line transmittance of the TAG ceramics with the wavelength from 300 to 1800 nm was measured with a UV-Vis-NIR spectrophotometer (Cary-5000, Varian, Palo Alto, CA, USA). The Verdet constant at 633 nm of the ceramics was determined at room temperature by an instrument consisting of a He-Ne laser, two polarizers, and an electromagnet.

3. Results and Discussion

The evolution of the chemical composition of the TAG precursor and nano-powders calcined at different temperatures was studied by XPS. The presence of the following elements on the TAG precursor and nano-powder surfaces was determined: C, O, Al, and Tb (Figure 1). There is also a small amount of fluorine (up to 3 at%), which was attributed to the abrasion of the polytetrafluoroethylene stirrer used in the precursor synthesis process. The signal from sulfur was not found as the most intensive line S 2p (169.5 eV) overlaps with Tb 4d, and analysis of the less intensive S 2s line (~230 eV) shows that sulfur concentration is less than 1at%. The surface chemical composition determined from photoelectron lines C 1s, O 1s, Al 2p, Tb 4d and the positions of the resolved lines are reported in Table 1.

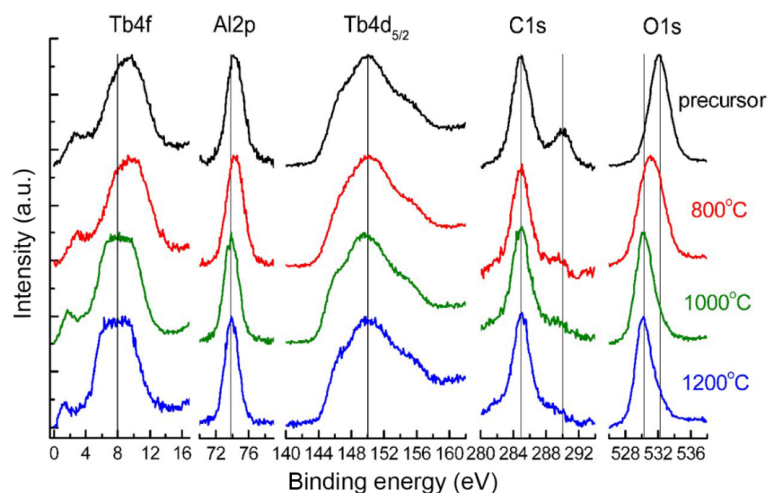


Figure 1. XPS of TAG precursor and nano-powders calcined at different temperatures.

Table 1. Surface chemical composition (at.%) and position (binding energy, eV) of resolved lines.

Sample		C 1s		O 1s		Tb 4d _{5/2}	Tb 4f	Al 2p
precursor	Line position (eV)	285.0	290.0	532.3		150.0	9.0	74.3
	Chemical composition (at%)	-	16.8	63.1		4.4	-	15.7
800 °C	Line position (eV)	285.0	290.0	530.8		150.0	9.0	74.3
	Chemical composition (at%)	-	5.6	60.2		6.8	-	27.4
900 °C	Line position (eV)	285.0	290.0	530.8		150.0	9.0	74.2
	Chemical composition (at%)	-	4.3	60.0		6.8	-	28.9
1000 °C	Line position (eV)	285.0	290.0	530.4	532.3	150.0	8.0	73.9
	Chemical composition (at%)	-	1.6	59.3		7.2	-	31.9
1100 °C	Line position (eV)	285.0	290.0	530.4	532.3	150.0	8.0	73.9
	Chemical composition (at%)	-	1.6	60.2		7.6	-	30.5
1200 °C	Line position (eV)	285.0	290.0	530.4	532.3	150.0	8.0	73.9
	Chemical composition (at%)	-	0	61.0		8.1	-	30.8

The C 1s line from the precursor surface has two components. The first component with a binding energy of 285 eV is connected with hydrocarbon contamination adsorbed from the atmosphere and is not taken into account in determining the surface composition. The second component with a binding energy of 290 ± 0.2 eV is usually connected with carbon bonded to oxygen (CO_3^{2-} , CO_2OH^- , CO^- , and so on) [44]. After calcining at 800 °C, the intensity of the second component sharply decreases and the concentration of this carbon component falls to zero at higher temperatures.

The O 1s line of the precursor has a binding energy (532.1 ± 0.2 eV) corresponding to the same bonds with carbon and hydrogen [45]. After calcining at 800 °C, the second component at a binding energy of 530.0 ± 0.2 eV appears, which is connected with the Me-O bond. Then, after calcination at more than 1000 °C, the concentration of the component with the higher binding energy decreases practically to zero.

The position and shape of the Tb 4d_{5/2} spin-orbital doublet do not change after calcining. The Tb 4f line close to the valence band shifts to a lower binding energy after calcining at 1000 °C and does not change at higher temperatures. For powders calcined at more than 1000 °C, the binding energy and shape of the Tb 4d_{5/2} line (150.0 ± 0.2 eV) correspond to terbium oxide, and the Tb 4f line is broader than that of terbium oxide [46].

During the calcining of the precursor, the Al 2p line position shifts to a lower binding energy, which indicates the formation of compounds with a less ionic chemical bond. For powders calcined above 1000 °C, the Al 2p line binding energy (73.9 ± 0.2 eV) corresponds to YAG [47], whose structure is similar to TAG. Hence, XPS analysis shows that TAG forms after calcination at about 1000 °C. The difference in the stoichiometric ratio of Tb and Al in the composition of the samples (Table 1) is attributed to the error in the calculation when using the tabular value of the Tb 4d line sensitivity factor, or the presence on the surface of the powders of an aluminum-enriched phase. In conclusion, XPS analysis shows that the concentration of elements does not change significantly when the calcination temperature is higher than 1000 °C, as shown in Figure 2.

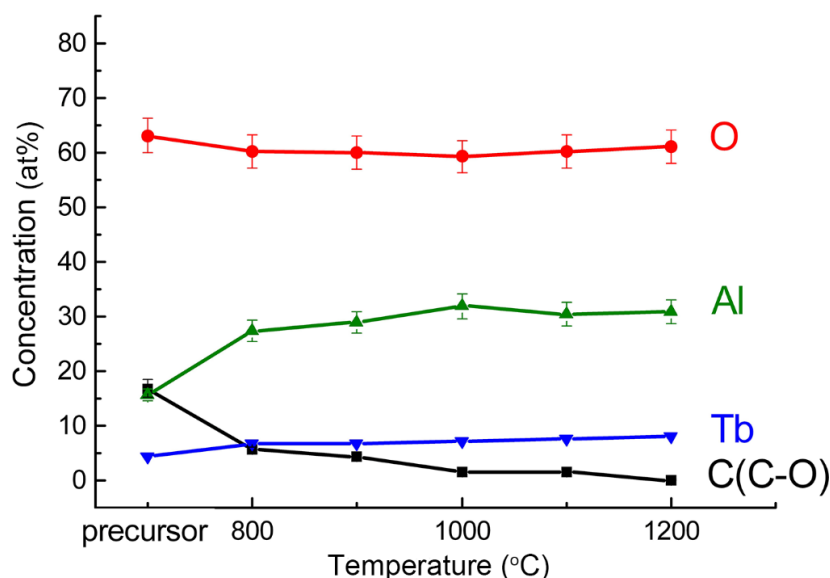


Figure 2. Atomic concentration of elements versus calcination temperature.

TG-DTA measurements were performed to analyze the thermal decomposition process of the precursor and the results are shown in Figure 3. As the precipitant is ammonium bicarbonate, the precursor is mainly composed of terbium and aluminum hydroxide, and basic carbonate. It can be seen from the thermogravimetric curve that the decomposition process of the precursor can be roughly divided into three steps, with a total weight loss of about 36%. The first thermal decomposition process occurs between room temperature and 500 °C. There is a wide and strong endothermic peak at 112 °C, which is mainly caused by

the volatilization of ethanol and adsorbed water in the precursor and the decomposition of hydration water and residual ammonium. As the temperature increases, a weight loss of about 5% occurs in the 500–1000 °C range, which is mainly attributed to the decomposition of hydroxides and carbonates [48]. The exothermic peak at about 919 °C is the formation of the TAG phase. No other exothermic peaks, for example, $Tb_4Al_2O_9$ (TAM) or $TbAlO_3$ (TAP) formation peaks, can be seen near this temperature, which means a good element uniformity in the precursor. As the temperature continues to rise, there is a weak weight loss above 1000 °C, accompanied by a small endothermic peak near 1139 °C, which represents the decomposition of SO_4^{2-} in the precursor. This shows that the detection of sulfur in XPS is indeed interfered with by the Tb 4d spectral line and an accurate result is not obtained. No significant weight loss was observed above ~1140 °C, indicating that the precursor has been completely decomposed. During the calcination process, the precursor decomposes and TAG particles crystallize. When the powder calcination temperature is too low, the precursor may decompose incompletely and some impurities may remain. Conversely, when the calcination temperature is too high, particles grow and agglomerate seriously, which reduces the formability and sintering activity. According to the analysis of XPS, TG-DTA results, and our previous studies [48], 1100 °C is selected as the subsequent powder calcination temperature.

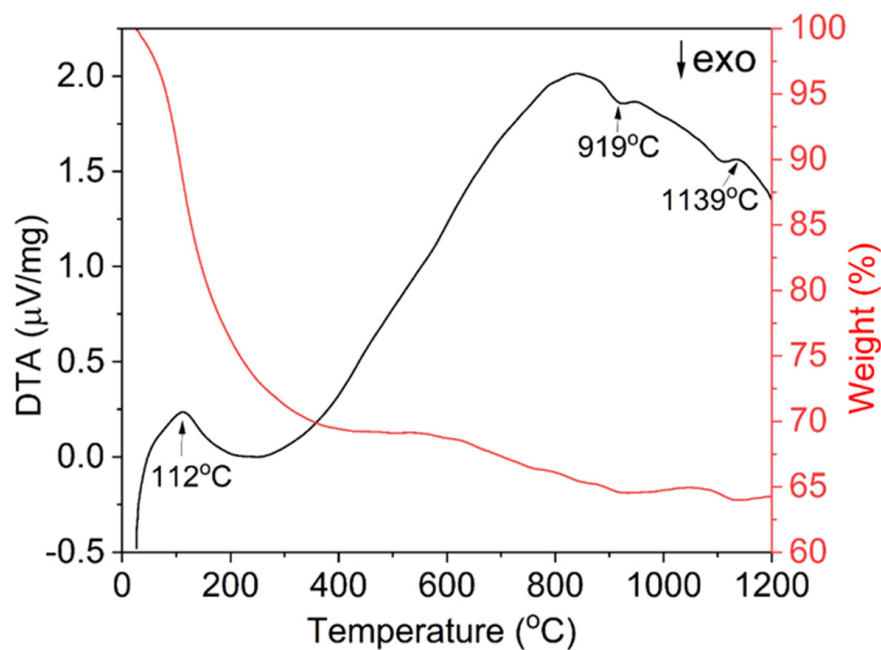


Figure 3. TG-DTA curves of TAG precursor synthesized by the co-precipitation method.

Figure 4 shows the XRD patterns of the synthesized precursor and calcined powder. Due to the low crystallization driving force in the co-precipitation process, the precursor is amorphous and no obvious diffraction peaks can be observed. After calcination at 1100 °C for 4 h, the precursor containing hydroxide, basic carbonate, and sulfide decomposes and forms a TAG phase with good crystallinity. All diffraction peaks of the calcined powders correspond to the standard card JCPDS#76-0111, confirming that the cubic TAG phase has been obtained.

Figure 5 shows the FESEM micrographs of the synthesized precursor and calcined powders. It can be seen that the precursor is mainly composed of near-spherical nanoparticles and they form submicron aggregates due to high surface energy. After air calcination at 1100 °C for 4 h, the morphology of TAG particles becomes dumbbell shaped and the particles have relatively uniform size distribution and good dispersion. In general, these results indicate the synthesized TAG powders are beneficial to obtaining uniform green bodies and the subsequent transparent ceramics.

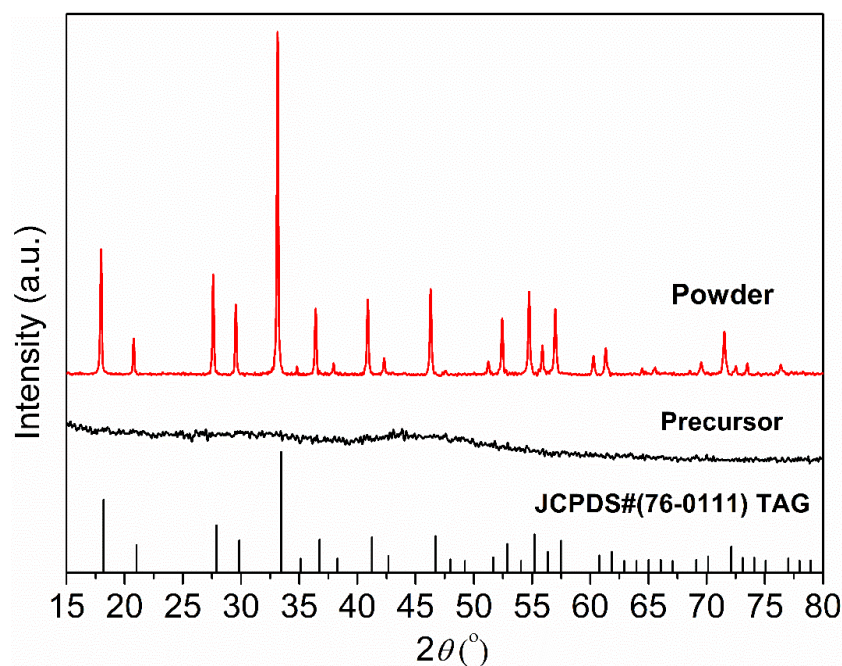


Figure 4. XRD patterns of the precursor and TAG powder calcined at 1100 °C for 4 h.

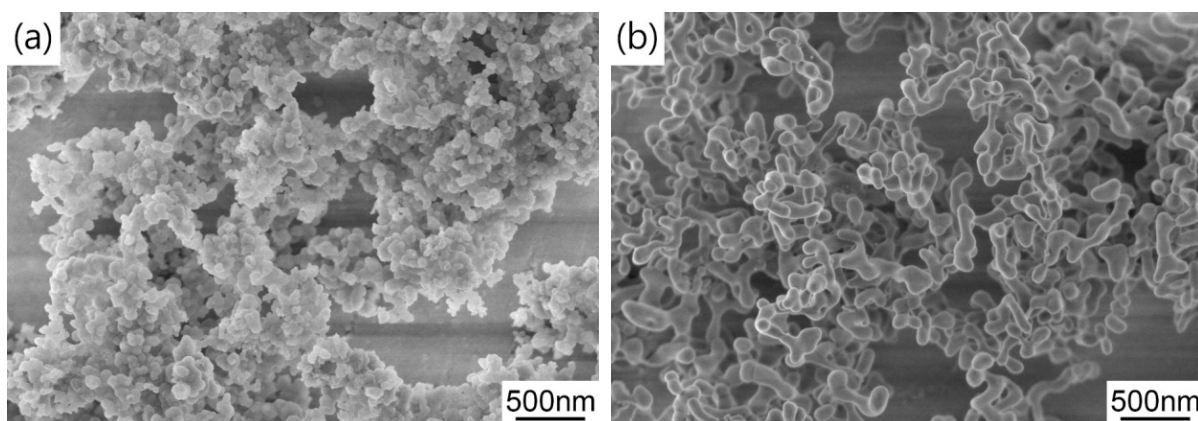


Figure 5. FESEM images of the (a) precursor and (b) powder calcined at 1100 °C for 4 h.

For the sake of obtaining pre-sintered ceramics with appropriate density and microstructure, the green bodies were sintered at 1400–1475 °C for 3 h in air. Figure 6 shows the average grain size and relative density of TAG ceramics pre-sintered at different temperatures. Two densification processes can be noticed in the range of 1400–1435 °C and 1435–1475 °C. In the first stage, the relative density of the TAG ceramics increases rapidly from 82.8% to 94.6%. Figure 7 shows the FESEM micrographs of TAG ceramics pre-sintered at different temperatures. The interconnected pores transform into isolated pores from 1400 °C to 1435 °C. There is only a slight increase in grain size, from 0.75 to 1.06 μm , due to the low temperature and pinning effect of pores. When the pre-sintering temperature is 1435–1475 °C, the densification rate of the TAG ceramics has slowed, and the relative density only increases from 94.6% to 96.8%. In the absence of pores and driven by high temperature, the grain size shows a rapid growth trend, and the grain size increases from 1.06 to 2.26 μm . This is conducive to obtaining transparent ceramics after HIP post-treatment from fine-grained pre-sintered ceramics without open pores or intragranular pores. According to the above results, a series of TAG ceramics with appropriate relative density and microstructure has been obtained by air pre-sintering at different temperatures.

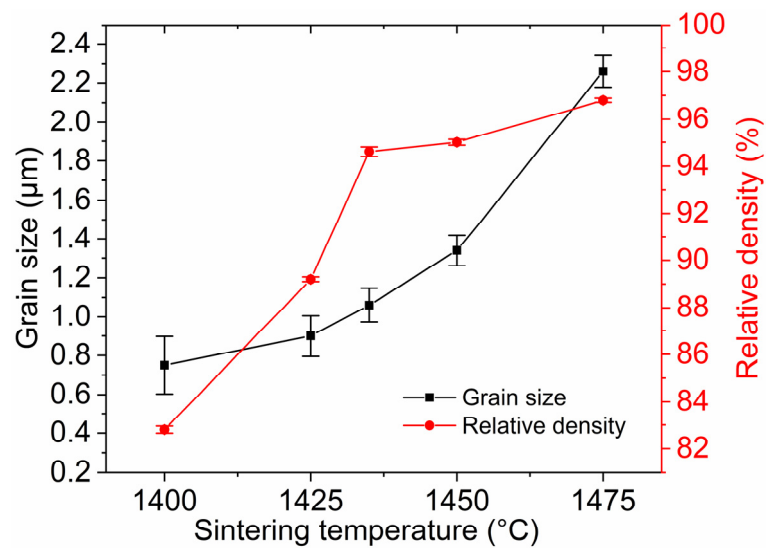


Figure 6. Average grain size and relative density of TAG ceramics as a function of pre-sintering temperature.

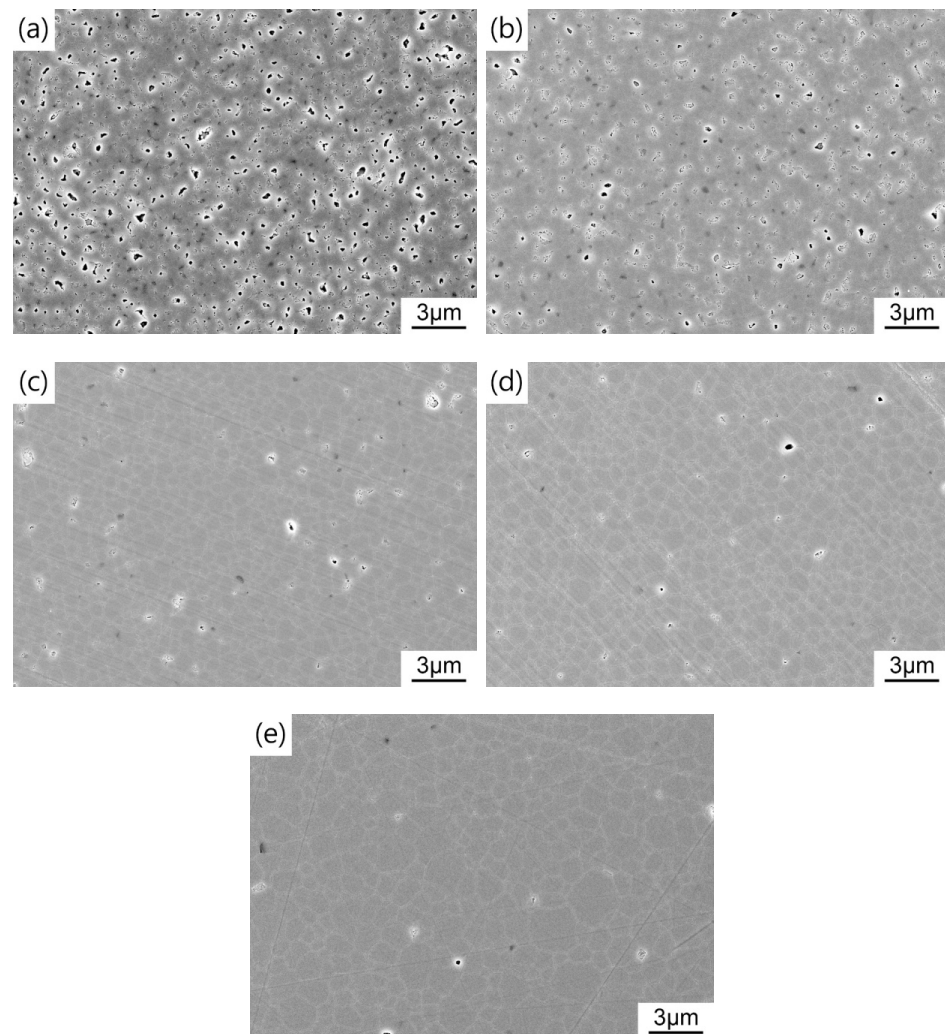


Figure 7. FESEM images of TAG ceramics air pre-sintered at different temperatures: (a) 1400 °C; (b) 1425 °C; (c) 1435 °C; (d) 1450 °C; (e) 1475 °C.

Figure 8 shows photographs and in-line transmission curves of the TAG ceramics fabricated by the two-step sintering process based on the low-temperature sintering process. Except for the ceramics air pre-sintered at 1400 °C, which are opaque after HIP treatment, the other TAG ceramics have a certain optical quality and the font under the ceramics can be observed. When the pre-sintering temperature is 1425 °C, the TAG ceramics after HIP post-treatment show a state of being transparent in the middle and opaque at the edge, due to the open pores at the edge of the pre-sintered body. In pace with the increase in air pre-sintering temperature, the optical quality of TAG ceramics after HIP post-treatment increases first and then decreases. When the pre-sintering temperature is 1450 °C, the optical quality of the annealed TAG ceramics is the optimum, and the in-line transmittance is about 80.3% at 1064 nm (the theoretical transmittance is 82.4% at 1064 nm [17]). However, the in-line transmittance of the ceramics at 633 nm is only 69.4% due to Rayleigh scattering, which may originate from the existence of scattering centers such as residual pores.

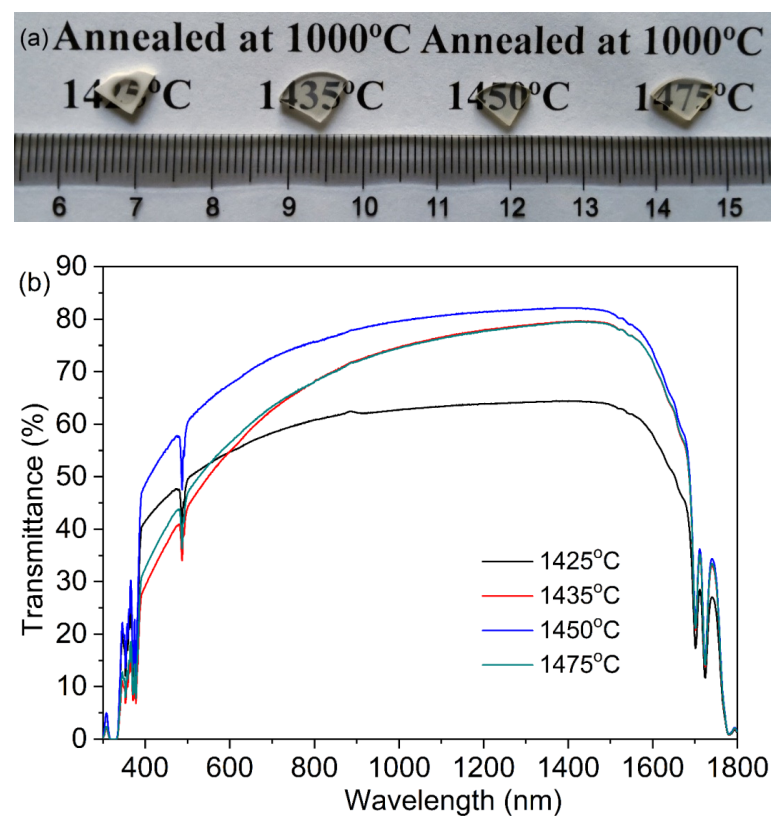


Figure 8. Photographs (a) and in-line transmission curves (b) of the TAG ceramics air pre-sintered at 1425–1475 °C for 3 h and HIP post-treated at 1550 °C for 3 h under a 176 MPa Ar atmosphere.

Figure 9 shows the microstructure of the HIP post-treated TAG ceramics prepared at different pre-sintering temperatures. When the pre-sintering temperature is 1400 °C, there are a large number of pores in the ceramics after HIP post-treatment, resulting in poor optical quality. The open pores during the HIP stage results in argon infiltrating the pores and eliminating the driving force for densification. When the pre-sintering temperature is 1425 °C, the TAG ceramics after HIP post-treatment is transparent in the middle and opaque at the edge. The corresponding microstructure is that the middle part is almost dense, while the edge part has a large number of pores (as shown in the inset of Figure 9b). Notably, the small white spots on the surface of the TAG ceramics are unwashed impurities, not the secondary phase. With the increase in pre-sintering temperature, the TAG ceramics after HIP post-treatment become uniform and dense, but there are still a few pores in the ceramics, which leads to the decline in the optical quality of the ceramics in the visible wavelength band. With the gradually increasing temperature, the average grain sizes of

the resulting TAG ceramics are 4.4, 5.2, 5.3, and 5.3 μm , respectively, which is smaller than that of TAG ceramics fabricated by vacuum sintering with higher temperature and longer holding time in most works [37,49,50]. Fine-grained ceramics usually possess better mechanical properties and better laser heat-related service performances. Air pre-sintering is also a more cost-effective choice compared with vacuum pre-sintering. Considering the current imperfect in-line transmittance, follow-up studies may focus on improving the optical quality by optimizing the powder morphology, choice and amount of sintering additive, pre-sintering parameters, and HIP conditions.

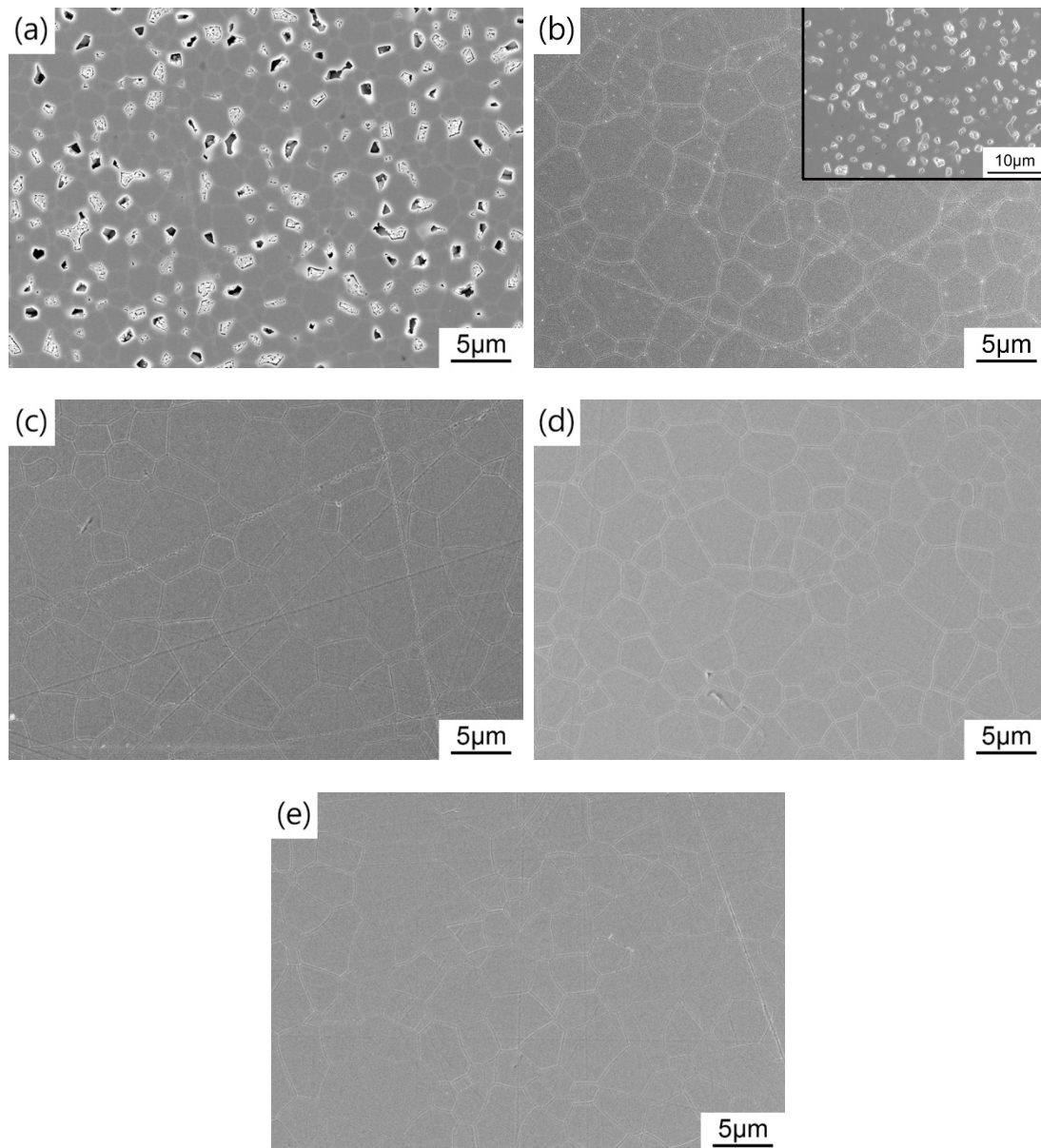


Figure 9. FESEM micrographs of the TAG ceramics sintered at (a) 1400 °C; (b) 1425 °C; (c) 1435 °C; (d) 1450 °C and (e) 1475 °C for 3 h and HIP post-treated at 1550 °C for 3 h.

The Verdet constant of the TAG ceramics at 632.8 nm is evaluated using the extinction method. As the optical quality has little effect on the Verdet constant of magneto-optical ceramics, the Verdet constants of all the TAG transparent ceramics are tested and the average value is calculated. The Verdet constant of the TAG ceramics is about $-180.5 \text{ rad}\cdot\text{T}^{-1}\cdot\text{m}^{-1}$, which is 1.3 times that of the commercial TGG crystals ($-134 \text{ rad}\cdot\text{T}^{-1}\cdot\text{m}^{-1}$). This superiority makes TAG ceramics a promising alternative material applied in the visible-to-near-infrared band.

4. Conclusions

On the basis of low-temperature sintering, transparent TAG ceramics with fine grains were prepared successfully by two-step sintering. The chemical compositions of the TAG precursor and calcined powder were analyzed in detail. In order to meet the requirements of HIP post-treatment, the microstructure evolution and relative density of air-pre-sintered TAG ceramics at different temperatures were studied. When the pre-sintering temperature is 1450 °C, the TAG ceramics after HIP post-treatment possess a small grain size of 5.3 μm and the highest in-line transmittance of 80.3% at 1064 nm. Air pre-sintering is proved to be a practical process for the fabrication of fine-grained TAG ceramics. The Verdet constant of the TAG ceramics is about $-180.5 \text{ rad} \cdot \text{T}^{-1} \cdot \text{m}^{-1}$ at 632.8 nm, which is about 30% higher than that of commercial TGG single crystals. Fine grains will give TAG ceramics better reliability, machinability, and performance in high-laser-power Faraday isolators, and further work may concentrate on optimizing the optical quality.

Author Contributions: Conceptualization, methodology and investigation, J.L., X.L. and L.Z.; validation, L.Z., D.H. and Z.D.; formal analysis, writing—original draft preparation and visualization, X.L., M.D. and R.Y.; writing—review and editing, L.Z., T.X. and Q.Y.; supervision, J.L., H.C., R.Y. and Q.L.; resources, project administration and funding acquisition, J.L. All authors have read and agreed to the published version of the manuscript.

Funding: This work was supported by the General Project of Shanghai Natural Science Foundation (Grant No. 22ZR1471500), the International Partnership Program of the Chinese Academy of Sciences (Grant No. 121631KYSB20200039), and the International Cooperation Project of Shanghai Science and Technology Commission (Grant No. 20520750200).

Institutional Review Board Statement: Not applicable.

Informed Consent Statement: Not applicable.

Data Availability Statement: Not applicable.

Conflicts of Interest: The authors declare no conflict of interest.

References

1. Dai, J.W.; Pan, Y.B.; Chen, H.H.; Xie, T.F.; Kou, H.M.; Li, J. Fabrication of $\text{Tb}_3\text{Al}_5\text{O}_{12}$ transparent ceramics using co-precipitated nanopowders: The influence of ammonium hydrogen carbonate to metal ions molar ratio. *Ceram. Int.* **2017**, *43*, 14457–14463. [[CrossRef](#)]
2. Yakovlev, A.; Snetkov, I.; Palashov, O. Thermo-optical properties of cryogenically cooled $(\text{Tb}_{0.9}\text{Y}_{0.1})_2\text{O}_3$ ceramics. *Opt. Commun.* **2022**, *504*, 127508. [[CrossRef](#)]
3. Zhang, L.X.; Li, X.Y.; Hu, D.J.; Liu, Z.Y.; Xie, T.F.; Wu, L.X.; Yang, Z.X.; Li, J. Fabrication and properties of non-stoichiometric $\text{Tb}_2(\text{Hf}_{1-x}\text{Tb}_x)_2\text{O}_{7-x}$ magneto-optical ceramics. *J. Adv. Ceram.* **2022**, *11*, 784–793. [[CrossRef](#)]
4. Zou, S.; He, X.Y.; Zeng, X.; Qiu, P.S.; Ling, L.; Sun, D.Z. Microstructure and properties of Bi-doped yttrium iron garnet magneto-optical ceramics prepared by hot-pressing sintering process. *J. Inorg. Mater.* **2022**, *37*, 773–779. [[CrossRef](#)]
5. Palashov, O.V.; Starobor, A.V.; Perevezentsev, E.A.; Snetkov, I.L.; Mironov, E.A.; Yakovlev, A.I.; Balabanov, S.S.; Permin, D.A.; Belyaev, A.V. Thermo-optical studies of laser ceramics. *Materials* **2021**, *14*, 3944. [[CrossRef](#)]
6. Golovina, T.G.; Konstantinova, A.F.; Evdishchenko, E.A. Magneto-optical effects in various crystalline materials, films, and meso- and nanostructures. *Crystallogr. Rep.* **2021**, *66*, 323–348. [[CrossRef](#)]
7. Li, J.; Dai, J.W.; Pan, Y.B. Research progress on magneto-optical transparent ceramics. *J. Inorg. Mater.* **2017**, *33*, 1–8. [[CrossRef](#)]
8. Dai, J.W.; Snetkov, I.L.; Palashov, O.V.; Pan, Y.B.; Kou, H.M.; Li, J. Fabrication, microstructure and magneto-optical properties of $\text{Tb}_3\text{Al}_5\text{O}_{12}$ transparent ceramics. *Opt. Mater.* **2016**, *62*, 205–210. [[CrossRef](#)]
9. Huang, X.Y.; Zuo, L.; Li, X.Y.; Feng, Y.G.; Liu, X.; Chen, X.P.; Xie, T.F.; Yang, Z.X.; Wu, L.X.; Li, J. Fabrication and characterization of $\text{Tb}_3\text{Al}_5\text{O}_{12}$ magneto-optical ceramics by solid-state reactive sintering. *Opt. Mater.* **2020**, *102*, 109795. [[CrossRef](#)]
10. Li, X.Y.; Zhang, L.X.; Hu, D.J.; Zhu, D.Y.; Chen, P.H.; Dai, Z.F.; Wu, L.X.; Xie, T.F.; Chen, H.H.; Liu, Q.; et al. Fabrication and characterizations of $\text{Tb}_3\text{Al}_5\text{O}_{12}$ -based magneto-optical ceramics. *Int. J. Appl. Ceram. Technol.* **2022**, *20*, 1–7. [[CrossRef](#)]
11. Snetkov, I.L.; Voitovich, A.V.; Palashov, O.V.; Khazanov, E.A. Review of Faraday isolators for kilowatt average power lasers. *IEEE J. Quantum Electron.* **2014**, *50*, 434–443. [[CrossRef](#)]
12. Snetkov, I.; Starobor, A.; Palashov, O.; Balabanov, S.; Permin, D.; Rostokina, E. Thermally induced effects in a faraday isolator on terbium sesquioxide (Tb_2O_3) ceramics. *Opt. Mater.* **2021**, *120*, 111466. [[CrossRef](#)]
13. Snetkov, I.; Yakovlev, A.; Starobor, A.; Balabanov, S.; Permin, D.; Rostokina, E.; Palashov, O. Thermo-optical properties of terbium sesquioxide (Tb_2O_3) ceramics at room temperature. *Opt. Lett.* **2021**, *46*, 3592–3595. [[CrossRef](#)] [[PubMed](#)]

14. Lu, B.; Wu, S.F.; Cheng, H.M.; Ye, R.J.; Cai, X.Y.; Wang, M.Y.; Wang, Y. Binary transparent $(\text{Ho}_{1-x}\text{Dy}_x)_2\text{O}_3$ ceramics: Compositional influences on particle properties, sintering kinetics and Faraday magneto-optical effects. *J. Eur. Ceram. Soc.* **2021**, *41*, 2826–2833. [[CrossRef](#)]
15. Vojna, D.; Slezák, O.; Lucianetti, A.; Mocek, T. Verdet constant of magneto-active materials developed for high-power Faraday devices. *Appl. Sci.* **2019**, *9*, 3160. [[CrossRef](#)]
16. Dai, J.W.; Pan, Y.B.; Li, X.Y.; Xie, T.F.; Yang, Z.X.; Li, J. Fabrication and properties of $(\text{Tb}_{1-x}\text{Ce}_x)_3\text{Al}_5\text{O}_{12}$ magneto-optical ceramics with different doping concentrations. *Scr. Mater.* **2018**, *155*, 46–49. [[CrossRef](#)]
17. Aung, Y.L.; Ikesue, A. Development of optical grade $(\text{Tb}_x\text{Y}_{1-x})_3\text{Al}_5\text{O}_{12}$ ceramics as Faraday rotator material. *J. Am. Ceram. Soc.* **2017**, *100*, 4081–4087. [[CrossRef](#)]
18. Hamamoto, K.; Nishio, M.; Tokita, S.; Uehara, H.; Yanagitani, T.; Fujioka, K.; Yasuhara, R.; Kawanaka, J. Properties of TAG ceramics at room and cryogenic temperatures and performance estimations as a Faraday isolator. *Opt. Mater. Express* **2021**, *11*, 434–441. [[CrossRef](#)]
19. Liu, H.P.; Zhan, G.X.; Wu, G.H.; Song, C.G.; Wu, X.; Xu, Q.R.; Chen, X.; Hu, X.L.; Zhuang, N.F.; Chen, J.Z. Improved edge-defined film-fed growth of incongruent-melting $\text{Tb}_3\text{Al}_5\text{O}_{12}$ crystal with high magneto-optical and thermal performances. *Cryst. Growth Des.* **2019**, *19*, 1525–1531. [[CrossRef](#)]
20. Ikesue, A.; Aung, Y.L. Magneto-optical performance of $(\text{LuTb})_3\text{Al}_5\text{O}_{12}$ single crystal by SSCG method. *Opt. Mater. X* **2022**, *13*, 100139. [[CrossRef](#)]
21. Xin, X.H.; Hao, Y.K.; Liu, L.; Lv, J.A.; Zhang, J.; Fu, X.W.; Jia, Z.T.; Tao, X.T. $\text{Tb}_3\text{Al}_3\text{Ga}_2\text{O}_{12}$: A novel visible-infrared Faraday crystal exhibiting a superior magneto-optical performance. *Cryst. Growth Des.* **2022**, *22*, 5535–5541. [[CrossRef](#)]
22. Lin, H.; Zhou, S.M.; Teng, H. Synthesis of $\text{Tb}_3\text{Al}_5\text{O}_{12}$ (TAG) transparent ceramics for potential magneto-optical applications. *Opt. Mater.* **2011**, *33*, 1833–1836. [[CrossRef](#)]
23. Duan, P.P.; Liu, P.; Xu, X.D.; Wang, W.; Wan, Z.; Zhang, S.Y.; Wang, Y.Z.; Zhang, J. Fabrication of transparent $\text{Tb}_3\text{Al}_5\text{O}_{12}$ ceramics by hot isostatic pressing sintering. *J. Am. Ceram. Soc.* **2017**, *100*, 2893–2900. [[CrossRef](#)]
24. Chen, J.; Tang, Y.R.; Chen, C.; Hao, D.M.; Yi, X.Z.; Ao, G.; Tian, Y.N.; Zhou, S.M. Roles of zirconia-doping in the sintering process of high quality $\text{Tb}_3\text{Al}_5\text{O}_{12}$ magneto-optic ceramics. *Scr. Mater.* **2020**, *176*, 83–87. [[CrossRef](#)]
25. Zhelezov, D.; Starobor, A.; Palashov, O.; Chen, C.; Zhou, S. High-power Faraday isolators based on TAG ceramics. *Opt. Express* **2014**, *22*, 2578–2583. [[CrossRef](#)] [[PubMed](#)]
26. Starobor, A.; Palashov, O. The temperature dependence of thermo-optical properties of magneto-optical TAG ceramics doped with silicon and titanium. *Opt. Mater.* **2018**, *78*, 15–20. [[CrossRef](#)]
27. Yang, C.L.; Huang, J.Q.; Huang, Q.F.; Deng, Z.H.; Wang, Y.; Li, X.Y.; Zhou, Z.H.; Chen, J.; Liu, Z.G.; Guo, W. Optical, thermal, and mechanical properties of $(\text{Y}_{1-x}\text{Sc}_x)_2\text{O}_3$ transparent ceramics. *J. Adv. Ceram.* **2022**, *11*, 901–911. [[CrossRef](#)]
28. Chen, P.H.; Li, X.Y.; Tian, F.; Liu, Z.Y.; Hu, D.J.; Xie, T.F.; Liu, Q.; Li, J. Fabrication, microstructure, and properties of 8 mol% yttria-stabilized zirconia (8YSZ) transparent ceramics. *J. Adv. Ceram.* **2022**, *11*, 1153–1162. [[CrossRef](#)]
29. Kaminskii, A.A.; Akchurin, M.S.; Gainutdinov, R.V.; Takaichi, K.; Shirakava, A.; Yagi, H.; Yanagitani, T.; Ueda, K. Microhardness and fracture toughness of Y_2O_3 - and $\text{Y}_3\text{Al}_5\text{O}_{12}$ -based nanocrystalline laser ceramics. *Crystallogr. Rep.* **2005**, *50*, 869–873. [[CrossRef](#)]
30. Starobor, A.; Palashov, O.; Zhou, S. Thermo-optical properties of terbium-aluminum garnet ceramics doped with silicon and titanium. *Opt. Lett.* **2016**, *41*, 1510–1513. [[CrossRef](#)]
31. Hao, D.; Chen, J.; Ao, G.; Tian, Y.; Tang, Y.; Yi, X.; Zhou, S. Fabrication and performance investigation of Thulium-doped TAG transparent ceramics with high magneto-optical properties. *Opt. Mater.* **2019**, *94*, 311–315. [[CrossRef](#)]
32. Chen, J.; Lin, H.; Hao, D.M.; Tang, Y.R.; Yi, X.Z.; Zhao, Y.A.; Zhou, S.M. Exaggerated grain growth caused by ZrO_2 -doping and its effect on the optical properties of $\text{Tb}_3\text{Al}_5\text{O}_{12}$ ceramics. *Scr. Mater.* **2019**, *162*, 82–85. [[CrossRef](#)]
33. Dai, J.W.; Pan, Y.B.; Xie, T.F.; Kou, H.M.; Li, J. Highly transparent $\text{Tb}_3\text{Al}_5\text{O}_{12}$ magneto-optical ceramics sintered from co-precipitated powders with sintering aids. *Opt. Mater.* **2018**, *78*, 370–374. [[CrossRef](#)]
34. Dai, J.W.; Pan, Y.B.; Xie, T.F.; Kou, H.M.; Li, J. A novel $(\text{Tb}_{0.995}\text{Ho}_{0.005})_3\text{Al}_5\text{O}_{12}$ magneto-optical ceramic with high transparency and Verdet constant. *Scr. Mater.* **2018**, *150*, 160–163. [[CrossRef](#)]
35. Liu, Q.; Li, X.Y.; Dai, J.W.; Yang, Z.X.; Xie, T.F.; Li, J. Fabrication and characterizations of $(\text{Tb}_{1-x}\text{Pr}_x)_3\text{Al}_5\text{O}_{12}$ magneto-optical ceramics for Faraday isolators. *Opt. Mater.* **2018**, *84*, 330–334. [[CrossRef](#)]
36. Yakovlev, A.I.; Snetkov, I.L.; Palashov, O.V.; Dai, J.; Li, X.; Li, J. Magneto-optical and thermo-optical properties of Ce, Pr, and Ho doped TAG ceramics. *IEEE J. Quantum Electron.* **2019**, *55*, 1–8. [[CrossRef](#)]
37. Chen, J.; Zhou, S. Review of magneto-optic materials for high power laser isolators. *Infrared Laser Eng.* **2020**, *49*, 20201072. [[CrossRef](#)]
38. Kariybayev, Z.T.; Lisitsyn, V.M.; Mussakhanov, D.A.; Alpyssova, G.K.; Popov, A.I.; Polisadova, E.F.; Elsts, E.; Akilbekov, A.T.; Kukenova, A.B.; Kemere, M.; et al. Time-resolved luminescence of YAG:Ce and YAGG:Ce ceramics prepared by electron beam assisted synthesis. *Nucl. Instrum. Methods Phys. Res. Sect. B Beam Interact. Mater. At.* **2020**, *479*, 222–228. [[CrossRef](#)]
39. Kuntz, J.D.; Roberts, J.J.; Hough, M.; Cherepy, N.J. Multiple synthesis routes to transparent ceramic lutetium aluminum garnet. *Scr. Mater.* **2007**, *57*, 960–963. [[CrossRef](#)]
40. Permin, D.; Postnikova, O.; Balabanov, S.; Belyaev, A.; Koshkin, V.; Timofeev, O.; Li, J. Influence of SHS precursor composition on the properties of yttria powders and optical ceramics. *Materials* **2023**, *16*, 260. [[CrossRef](#)]

41. Lee, S.-H.; Kupp, E.R.; Stevenson, A.J.; Anderson, J.M.; Messing, G.L.; Li, X.; Dickey, E.C.; Dumm, J.Q.; Simonaitis-Castillo, V.K.; Quarles, G.J. Hot isostatic pressing of transparent Nd:YAG ceramics. *J. Am. Ceram. Soc.* **2009**, *92*, 1456–1463. [[CrossRef](#)]
42. Laguta, V.; Buryi, M.; Arhipov, P.; Sidletskiy, O.; Laguta, O.; Brik, M.G.; Nikl, M. Oxygen-vacancy donor-electron center in $Y_3Al_5O_{12}$ garnet crystals: Electron paramagnetic resonance and dielectric spectroscopy study. *Phys. Rev. B* **2020**, *101*, 024106. [[CrossRef](#)]
43. Chaika, M.; Vovk, O.; Mancardi, G.; Tomala, R.; Strek, W. Dynamics of Yb^{2+} to Yb^{3+} ion valence transformations in Yb:YAG ceramics used for high-power lasers. *Opt. Mater.* **2020**, *101*, 109774. [[CrossRef](#)]
44. Brent Siegbahn, K.; Nordling, C.; Fahlman, A.; Nordberg, R.; Hamrin, K.; Hedman, J.; Johansson, G.; Bergmark, T.; Karlsson, S.-E.; Lindgren, I.; et al. *ESCA: Atomic, Molecular and Solid State Structure Studied by Means of Electron Spectroscopy*; Almqvist and Wiksell: Upsala, Switzerland, 1967.
45. Barr, T.L. An ESCA study of the termination of the passivation of elemental metals. *J. Phys. Chem.* **1978**, *82*, 1801–1810. [[CrossRef](#)]
46. Teterin, Y.A.; Teterin, A.Y. Structure of X-ray photoelectron spectra of lanthanide compounds. *Russ. Chem. Rev.* **2002**, *71*, 347–381. [[CrossRef](#)]
47. Kosyanov, D.Y.; Yavetskiy, R.P.; Baumer, V.N.; Kopylov, Y.L.; Kravchenko, V.B.; Vorona, I.O.; Cherednichenko, A.I.; Vovna, V.I.; Tolmachev, A.V. Effect of Nd^{3+} ions on phase transformations and microstructure of 0–4 at.% $Nd^{3+}:Y_3Al_5O_{12}$ transparent ceramics. *J. Alloys Compd.* **2016**, *686*, 526–532. [[CrossRef](#)]
48. Dai, J.W.; Pan, Y.B.; Wang, W.; Luo, W.; Xie, T.F.; Kou, H.M.; Li, J. Fabrication of $Tb_3Al_5O_{12}$ transparent ceramics using co-precipitated nanopowders. *Opt. Mater.* **2017**, *73*, 38–44. [[CrossRef](#)]
49. Dai, J.W.; Li, J. Promising magneto-optical ceramics for high power Faraday isolators. *Scr. Mater.* **2018**, *155*, 78–84. [[CrossRef](#)]
50. Ikesue, A.; Aung, Y.L.; Wang, J. Progress of magneto-optical ceramics. *Prog. Quantum Electron.* **2022**, *86*, 100416. [[CrossRef](#)]

Disclaimer/Publisher’s Note: The statements, opinions and data contained in all publications are solely those of the individual author(s) and contributor(s) and not of MDPI and/or the editor(s). MDPI and/or the editor(s) disclaim responsibility for any injury to people or property resulting from any ideas, methods, instructions or products referred to in the content.